INTERFACE

Research

Check for updates

Author for correspondence:
Wei Sun
e-mail: wei.sun@bme.gatech.edu

THE ROYAL SOCIETY
PUBLISHING

A deep learning approach to estimate stress distribution: a fast and accurate surrogate of finite-element analysis

Liang Liang, Minliang Liu, Caitlin Martin and Wei Sun

Tissue Mechanics Laboratory, The Wallace H. Coulter Department of Biomedical Engineering, Georgia Institute of Technology and Emory University, Technology Enterprise Park, Room 206, 387 Technology Circle, Atlanta, GA 30313-2412, USA

(iD) WS, 0000-0002-8708-5128

Structural finite-element analysis (FEA) has been widely used to study the biomechanics of human tissues and organs, as well as tissue–medical device interactions, and treatment strategies. However, patient-specific FEA models usually require complex procedures to set up and long computing times to obtain final simulation results, preventing prompt feedback to clinicians in time-sensitive clinical applications. In this study, by using machine learning techniques, we developed a deep learning (DL) model to directly estimate the stress distributions of the aorta. The DL model was designed and trained to take the input of FEA and directly output the aortic wall stress distributions, bypassing the FEA calculation process. The trained DL model is capable of predicting the stress distributions with average errors of 0.492% and 0.891% in the Von Mises stress distribution and peak Von Mises stress, respectively. This study marks, to our knowledge, the first study that demonstrates the feasibility and great potential of using the DL technique as a fast and accurate surrogate of FEA for stress analysis.

1. Introduction

Stress analysis is the hallmark of mechanics. Numerical analysis methods, including structural finite-element analysis (FEA) and computational fluid dynamics (CFD), are used to perform stress analysis of complex structures and systems in which it may be difficult to obtain an analytical solution. These analyses can be used to evaluate design, maintenance and safety of complex structures in a wide array of applications across many industries including aerospace, automotive, architecture, and, more recently, are rapidly penetrating the biomedical engineering space. Advances in imaging techniques have made it possible to study the mechanics of human tissues and organs, as well as tissue–medical device interactions, and treatment strategies at a patient-specific level [1–9].

The current workflow for such patient-specific FEA applications is shown in figure 1: (i) patient anatomic geometries are obtained mostly through manual annotation of *in vivo* clinical image data (e.g. image region segmentation and object boundary delineation); (ii) an FE model is set up by specifying material properties and the boundary and loading conditions in the FE model, and (iii) the FE model is submitted as an FEA job, to a finite-element numerical solver to obtain simulation results, which, depending on the complexity of the model and application, may take anywhere from minutes [10] to days [11]. The complexity and time-consuming nature of the current workflow makes it impractical to apply patient-specific computational analyses in time-sensitive clinical applications, which require fast diagnosis and treatment planning.

To resolve these limitations, we hypothesize that a fully automatic patient-specific modelling workflow could be built upon machine learning (ML) techniques: a paradigm-changing ML solution that may render the stress analysis in a few seconds for time-sensitive clinical applications (figure 1). The ML
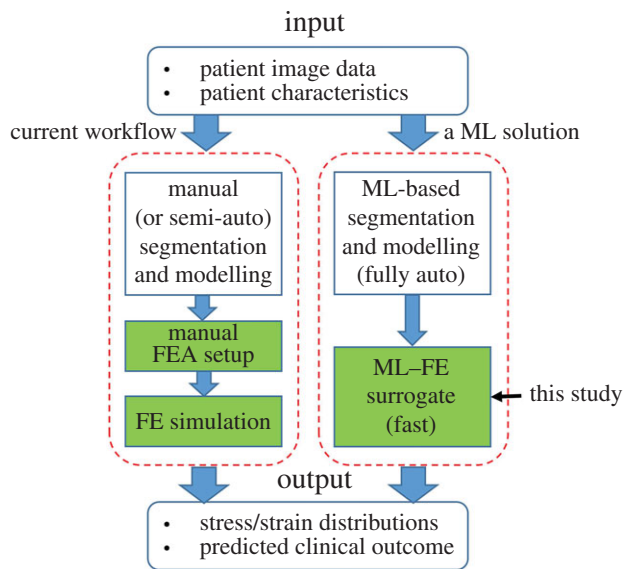
Figure 1. The current workflow versus a machine learning-based solution for patient-specific computational modelling for potential clinical applications. This study is focused on developing the ML−FE surrogate to replace FEA including model set-up and simulation.

workflow consists of (i) ML-based geometry reconstruction and modelling to directly output patient anatomical geometries from input patient raw clinical image data, and (ii) ML-based mechanical analysis to directly output FEA stress analysis results from the input anatomical model. By using ML techniques and deformable model fitting methods, the feasibility of automatic geometry reconstruction and modelling from images has been established for many applications [12–20], including aortic valve modelling [12,21]. However, currently the only way to perform stress analysis is through FEA. We propose to use deep learning (DL) techniques [22,23] to build deep neural networks (DNNs) as an FEA surrogate for mechanical stress analysis. DNNs are capable of modelling complex, nonlinear relationships between input and output variables; thus, given adequate *a priori* analysis data for training including anatomical models and FEA results, we hypothesize that DNNs could offer a potential solution to real-time patient-specific computational simulations, by enabling fast and accurate stress analysis.

In this study, we present, to our best knowledge, the first 'ML−FE surrogate' approach to perform fast and accurate stress analysis for biomedical applications. The approach is demonstrated in the application of stress analysis of the human thoracic aorta. Given an input shape, i.e. thoracic aorta geometry, the trained DL model can output the aortic wall stress distributions within 1 s, consistent with and magnitudes faster than FEA which takes about half an hour on the same computer.

2. Material and methods

2.1. Patient geometry and finite-element simulation dataset

In a previous study [10], we constructed a dataset of 729 thoracic aorta shapes and corresponding wall stress distributions, which was used to train and test the DL model. The thoracic aorta

shapes were generated from a statistical shape model (SSM) built upon real patient geometries, which can be considered as 729 virtual patient geometries. FEA was performed to obtain the stress distributions of each shape. Each shape is represented by a quadrilateral mesh with 5000 nodes and 4950 elements, as shown in figure 2. The mechanical behaviour of the aorta tissue was described by a fibre-reinforced hyperelastic material model [24], for which a set of material parameters was prescribed based on our previous experiment [25]. The FE simulations were performed using Abaqus/Standard 6.14 (Simulia, RI), and the stress distributions under the systolic pressure of 16 KPa were output and recorded for each shape model. The details of patient image data collection, virtual patient geometries and FEA are provided in [10] and the appendix.

2.2. Deep learning model

The overall data flow of the DL model is shown in figure 3. Given an input shape, it will output the wall stress distributions in the following three steps: (i) encode the input shape as a set of scalar values, i.e. shape code; (ii) conduct a nonlinear mapping of the shape code to the stress code represented by a set of scalar values; and (iii) decode the stress code into wall stress distributions. The details of each step of the DL model are described in the following sections.

2.2.1. Aorta shape encoding

Shape encoding refers to a method of representing a shape by a small number of scalar values. There are several methods available for shape encoding, including principal component analysis (PCA), independent component analysis and sparse coding [13]. Among these methods, PCA is widely used in statistical shape analysis [26] and was chosen as the shape encoding method in this study. By using PCA, a shape X can be represented by

$$X \cong X_{\text{PCA}} = \bar{X} + \sum_{m=1}^{M} \alpha_m \sqrt{\lambda_m} W_m, \tag{2.1}$$

where $\bar{X}$ is the mean shape, and $\{W_m\}$ and $\{\lambda_m\}$ are the eigenvectors (i.e. modes of shape variations) and eigenvalues of the covariance matrix, respectively. By using equation (2.1) and the fact that eigenvectors are orthogonal to each other, the shape code $\{\alpha_m\}$ of the aorta X can be obtained by

$$\alpha_m = \frac{W_m^{\text{T}}(X - \bar{X})}{\sqrt{\lambda_m}} \tag{2.2}$$

where W_m^{T} is the transpose of the column vector W_m, and $m = 1, 2, 3$. Equation (2.2) is equivalent to a neural network with linear units and without hidden layers, as shown in figure 4. More details on PCA-based shape analysis can be found in the appendix and [10].

### 2.2.2. Nonlinear mapping from shape code to stress code

A multilayer neural network was designed to map the shape code $\{\alpha_m\}$ to the stress code $\{\beta_n\}$, which is essentially a nonlinear regression with high-dimensional input and output, i.e. establishing functions $\beta_n = f(\alpha_1, \ldots, \alpha_M)$ for every $n = 1, \ldots, N$. The structure of the neural network is shown in figure 5. It has two hidden layers, each of which has 128 units. As this is a nonlinear regression, softplus units [27] were used. We note that there are other types of nonlinear units [28] very similar to softplus, such as ReLU or Leaky ReLU, which may also be used for this task.

2.2.3. Aortic wall stress encoding and decoding

The stress distribution on the aortic wall can be represented (i.e. encoded) by and reconstructed (i.e. decoded) from a set of scalar
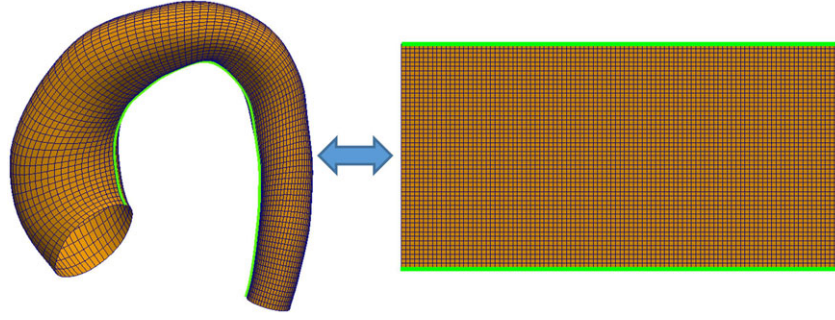
Figure 2. A representative aorta mesh, which is topologically equivalent to a rectangle.
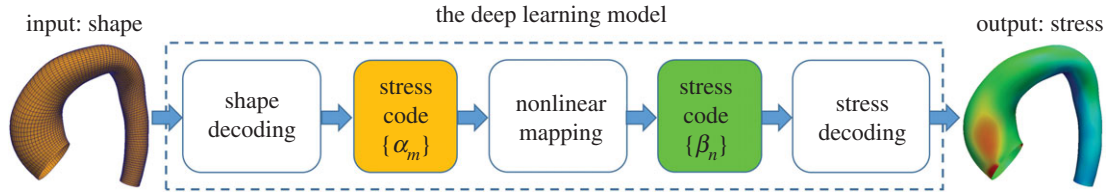
Figure 3. The overall data flow of the deep learning model which takes an aorta shape as the input and outputs the wall stress distribution.
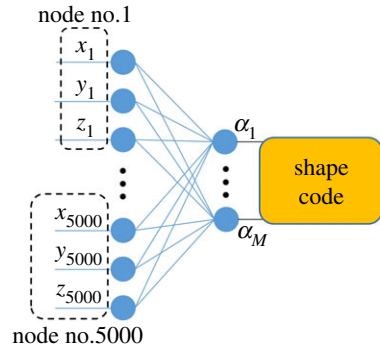
Figure 4. The neural network for shape encoding. (x_i, y_i, z_i) is equal to the node-i position of shape X minus the node-i position of the mean shape $\bar{X}$. The link (i.e. weight) between α_m and x_1 is the first component of $W_m/\sqrt{\lambda_m}$; the link between α_m and z_{5000} is the last component of $W_m/\sqrt{\lambda_m}$; and so on. In this application, $M = 3$ and each W_m has 15 000 components.
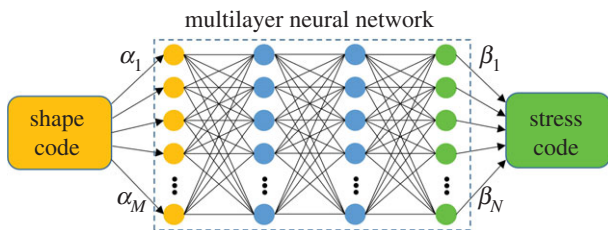
Figure 5. The neural network for mapping the shape code to the stress code. In this study, $M = 3$ and $N = 64$.

values. The encoding and decoding processes can be described conceptually by a bidirectional neural network with multiple layers and linear units, as shown in figure 6. Stress encoding was only used in the training stage, while stress decoding is a part of the DL model. To facilitate the processes, each aorta mesh was divided into 25 regions consisting of the same number of nodes (i.e. 200 nodes per region). Low rank approximation (LRA) [29] was used for stress encoding and decoding.

In the decoding process, the stress code $\{\beta_n\}$ of the whole aorta is converted into the stress code of each region of the aorta, given by

$$R = \sum_{n=1}^{64} \beta_n \mu_n U_n, \tag{2.3}$$

where $R = [R_{\text{region\_1}}^{\text{T}}, \ldots, R_{\text{region\_25}}^{\text{T}}]^{\text{T}}$ and $R_{\text{region\_k}} = [r_1^{(k)}, \ldots, r_{256}^{(k)}]^{\text{T}}$, which is the stress code for the kth region. From LRA performed on R, $\{U_n\}$ are the left-singular vectors, $\{\mu_n\}$ are the corresponding singular values and $\{\beta_n\}$ are the LRA parameters. The 64 most significant singular components were retained in the LRA, which led to an approximation error less than 1%. In each region, the stress distribution $S^{(k)}$ can be obtained by

$$S^{(k)} = \sum_{i=1}^{256} r_i^{(k)} \nu_i^{(k)} V_i^{(k)}. \tag{2.4}$$

From LRA performed on $S^{(k)}$, $\{V_i^{(k)}\}$ are the left-singular vectors, $\{\nu_i^{(k)}\}$ are the corresponding singular values and $\{r_i^{(k)}\}$ are the LRA parameters. The 256 most significant singular components were retained in the LRA, which led to an approximation error less than 1%. The column vector $S^{(k)}$ contains 600 stress values: three stress components at each node, and there are 200 nodes per region. The three stress components are S_{11} along the circumferential direction, S_{22} along the longitudinal direction and the shear stress S_{12}. As the other stress components are nearly zero, we can compute the Von Mises stress from S_{11}, S_{22} and S_{12}.

In the encoding process, the stress codes can be obtained by

$$r_i^{(k)} = \frac{\left(V_i^{(k)}\right)^{\text{T}} S^{(k)}}{\nu_i^{(k)}} \tag{2.5}$$

and $$\beta_n = \frac{U_n^{\text{T}} R}{\mu_n}, \tag{2.6}$$

which are based on equation (2.3) and (2.4) and the fact that singular vectors are orthogonal to each other.

To reduce the complexity of the module, we set the constraint on $V_i^{(k)}$ in equation (2.4): $V_i^{(k_1)} \equiv V_i^{(k_2)}$ for any k_1 and k_2, and thus the 25 subnetworks in figure 6 share the same weights. Therefore, the stress decoding module can be implicitly implemented as a neural network with transposed-convolution layers [28], and the stress encoding module can be implicitly implemented as a

bidirectional neural network

divide aortic wall
into 25 regions

1	2	3	4	5
6	7	8	9	10
11	12	13	14	15
16	17	18	19	20
21	22	23	24	25

200 nodes
per region

256 units
per region

600 stress
values
per region
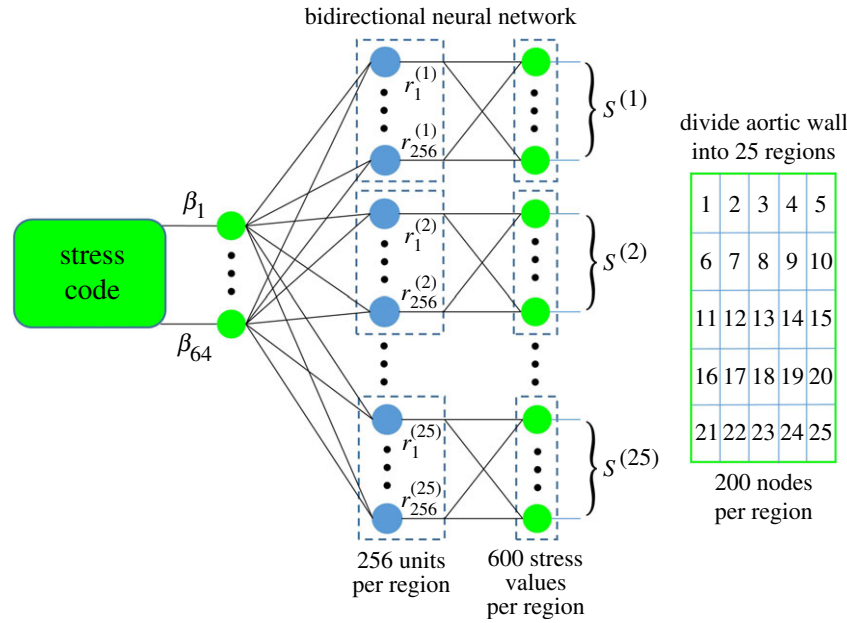
Figure 6. The bidirectional neural network for stress decoding (from left to right) and encoding (from right to left). It has 25 subnetworks, corresponding to the 25 regions of the aorta. The aorta mesh is equivalent to a rectangular mesh that is divided into 25 regions.

neural network with convolution layers [28]. Each constant $v_i^{(k)}$ can be absorbed into $r_i^{(k)}$. Weight sharing is a general strategy to reduce the complexity of a neural network using convolution and transposed-convolution operations [28].

2.3. Training of the deep learning model

The parameters of the DL model were learned from the training data. As the three modules of the DL model were designed for specific tasks, these modules were trained separately through a combination of unsupervised and supervised learning methods. The parameters of the shape encoding module and the stress encoding module were obtained using the PCA and LRA algorithms, which are unsupervised learning methods. After the two modules were trained, the parameters of the nonlinear mapping module were obtained through supervised learning by using a mean-square loss function and the Adamax optimization algorithm [30], to predict the stress code from the shape code, for which the stress code is obtained through stress-encoding. The Adamax algorithm performs stochastic optimization to find the optimal parameters of the nonlinear mapping module.

We note that the shape encoding module can also be described conceptually as a bidirectional neural network. Shape decoding is unnecessary because shape reconstruction from the shape code is not used in this study. The nonlinear mapping module is not bidirectional; and if the reader is interested in mapping the stress code back to the shape code, a completely different neural network needs to be designed and trained for this task. The stress decoding/encoding module is conceptually bidirectional, which implies that once the stress encoder is determined through LRA-based unsupervised learning, the stress decoder is also determined. In the implementation (i.e. computer code), two separated neural networks were used for stress encoding and decoding.

2.4. Evaluation of the deep learning model

The performance of the DL model was evaluated using a Monte Carlo cross-validation approach to test whether the trained model can recover the stress distributions. In each round of the cross-validation, 90% of the shapes and corresponding stress distributions were randomly selected as the training data to determine the parameters of the DL model; and the remaining

10% of the data were used as the testing data to obtain performance measures. The process was repeated 100 times to obtain the mean and standard deviation of each performance measure.

Two performance metrics were used to evaluate the accuracy of the estimated stress distributions from the DL model: mean absolute error (MAE) and normalized mean absolute error (NMAE). For each shape, the MAE is defined by

$$\text{MAE} = \frac{1}{5000} \sum_{i=1}^{5000} |S(i) - \tilde{S}(i)|, \quad (2.7)$$

where $S(i)$ is a stress value at node i computed from FEA, $\tilde{S}(i)$ is the corresponding stress estimated by the DL model and $|\,|$ denotes the absolute value. For each shape, the NMAE is defined by

$$\text{NMAE} = \frac{\text{MAE}}{\max\{|S|\}} \times 100\%, \quad (2.8)$$

where $\max\{|S|\}$ is the peak stress from FEA. By substituting S_{11} or S_{22} or S_{12} for S in equations (2.7) and (2.8), we can obtain accuracy metrics for the distributions of different stress components.

Two additional performance metrics were used to evaluate the accuracy of the estimated peak stress values from the DL model: absolute error (AE) and normalized absolute error (NAE). For each shape, the AE is defined by

$$\text{AE} = |\max\{|S|\} - \max\{|\tilde{S}|\}|, \quad (2.9)$$

where $\max\{|S|\}$ is the peak stress from FEA, and $\max\{|\tilde{S}|\}$ is the corresponding peak stress estimated by the DL model. For each shape, the NAE is defined by

$$\text{NAE} = \frac{\text{AE}}{\max\{|S|\}} \times 100\%. \quad (2.10)$$

When calculating $\max\{|S|\}$ and $\max\{|\tilde{S}|\}$, stress values at five layers of elements adjacent to the mesh boundaries were excluded in order to avoid boundary effects. By substituting S_{11} or S_{22} or S_{12} for S in equations (2.9) and (2.10), we can obtain accuracy metrics for the peak value of different stress components.

Table 1. The accuracy of the estimated stress distributions.

	S_{11}	S_{22}	S_{12}	Von Mises
MAE (KPa)	1.573 ± 1.048	0.956 ± 0.521	0.658 ± 0.226	1.366 ± 0.906
NMAE	$0.502 \pm 0.347\%$	$0.639 \pm 0.362\%$	$1.739 \pm 0.665\%$	$0.492 \pm 0.336\%$

Table 2. The accuracy of the estimated peak stress values.

	peak S_{11}	peak S_{22}	peak S_{12}	peak Von Mises
AE (KPa)	2.807 ± 2.518	1.623 ± 3.244	1.611 ± 2.501	2.513 ± 2.447
NAE	$0.885 \pm 0.792\%$	$1.030 \pm 1.527\%$	$3.654 \pm 3.564\%$	$0.891 \pm 0.838\%$

3. Results

The proposed DL model was trained and tested on a dataset of 729 aorta geometries and stress distributions. As unsupervised learning methods were used to determine the parameters of the shape encoding module and the stress decoding module, training of the entire DL model was very fast (approx. 5 min for each round in the cross-validation). The stress values computed by FEA were considered the ground truth, which were compared to the stress values predicted by the DL model. The performance of the DL model was evaluated in 10-fold cross-validation. The details of the methods, data and performance metrics are described in §2. The accuracy measures of the estimated stress distributions are reported in table 1, and the accuracy measures of the estimated peak stress values are reported in table 2. The components of a stress tensor are S_{11} along the circumferential direction, S_{22} along the longitudinal direction and the shear stress S_{12}. The Von Mises stress can be calculated from these stress components. The accuracy of the DL model-predicted Von Mises stress distributions were evaluated by comparing to the FEA-predicted distributions: an average MAE of 1.366 KPa and an average NMAE of 0.492% were obtained. The estimated shear stress distribution, S_{12}, had the smallest average MAE of 0.658 KPa and the largest average NMAE of 1.739% because the magnitude of S_{12} is very small compared to that of S_{11} or S_{22}.

The results are visualized for two representative aortic shapes shown in figure 7 and figure 8, and the accuracy measures are reported in table 3 and table 4, respectively. For the shape shown in figure 7, the NMAE of the estimated Von Mises stress distribution is 0.078%, much smaller than the mean error, and there is almost no discrepancy between the stress computed by FE and the stress estimated by the DL model. For the shape shown in figure 8, the NMAE of the estimated Von Mises stress distribution is 1.131%, which represents one of the worst predictions. Although there are some subtle differences, the overall stress distributions are very similar.

The DL model was implemented using Matlab and Tensorflow [31]. Given an input shape, the DL model can output the stress distributions within 1 s (excluding initialization and file IO time) on a PC with a 3.6 GHz quad core CPU and 32 GB RAM. As a comparison, it took approximately 30 min for FEA to obtain the stress distributions for the same input, and it could be much longer when numerical convergence issues are encountered in some cases and thus human experts are needed to manually adjust FE solver parameters in order to solve the problem in a trial and error fashion. Once the FEA input–output relationship was learned by the DL model, FEA was no longer needed, i.e. replaced by the DL model.

4. Discussion

In this study, we proposed to use an ML–FE surrogate to directly estimate the aortic wall stress distributions given the geometry and material properties of the aorta. To this end, we developed a DL model with a novel structure that consists of three modules: shape encoding, nonlinear mapping and stress decoding, which were trained using a combination of supervised and unsupervised learning methods. The developed DL model was evaluated through cross-validation, where an average discrepancy of 0.492% (NMAE) was achieved between FE-computed and DL-estimated Von Mises stress distributions. Thus, the stress distributions estimated by the ML–FE surrogate are highly consistent with those from FEA. To our best knowledge, this is the first study in which DL techniques were used to quickly and accurately predict FEA results. This work was motivated by the lengthy and complex nature of nonlinear FEA on the human aorta. In our recent work [10], it took approximately 30 min to estimate an unpressurized geometry and then to inflate the unpressurized geometry to the target pressure level to obtain the stress distributions for a given human aorta geometry, whereas the stress distributions could be obtained within one second (on the same PC) with the DL model of this study. The success of this study holds promise for the use of ML techniques to expedite the patient-specific mechanical analysis of human soft tissues and organs by bypassing the time-consuming model construction and simulation processes.

ML techniques, especially DNNs, have been applied in a few studies [32–34] to speed up CFD computation, and in a few biomechanics applications with the intent to learn from computational simulations and predict certain clinical parameters. For example, Itu and co-workers [35] proposed a method to measure fractional flow reserve (FFR) from coronary computed tomography, where an ML model was trained on a synthetic FFR dataset obtained from the CFD method. Our group proposed a ML approach [10] to assess the pressure rupture risk of thoracic aortic aneurysm, where ML models were trained on the virtual patient aneurysm
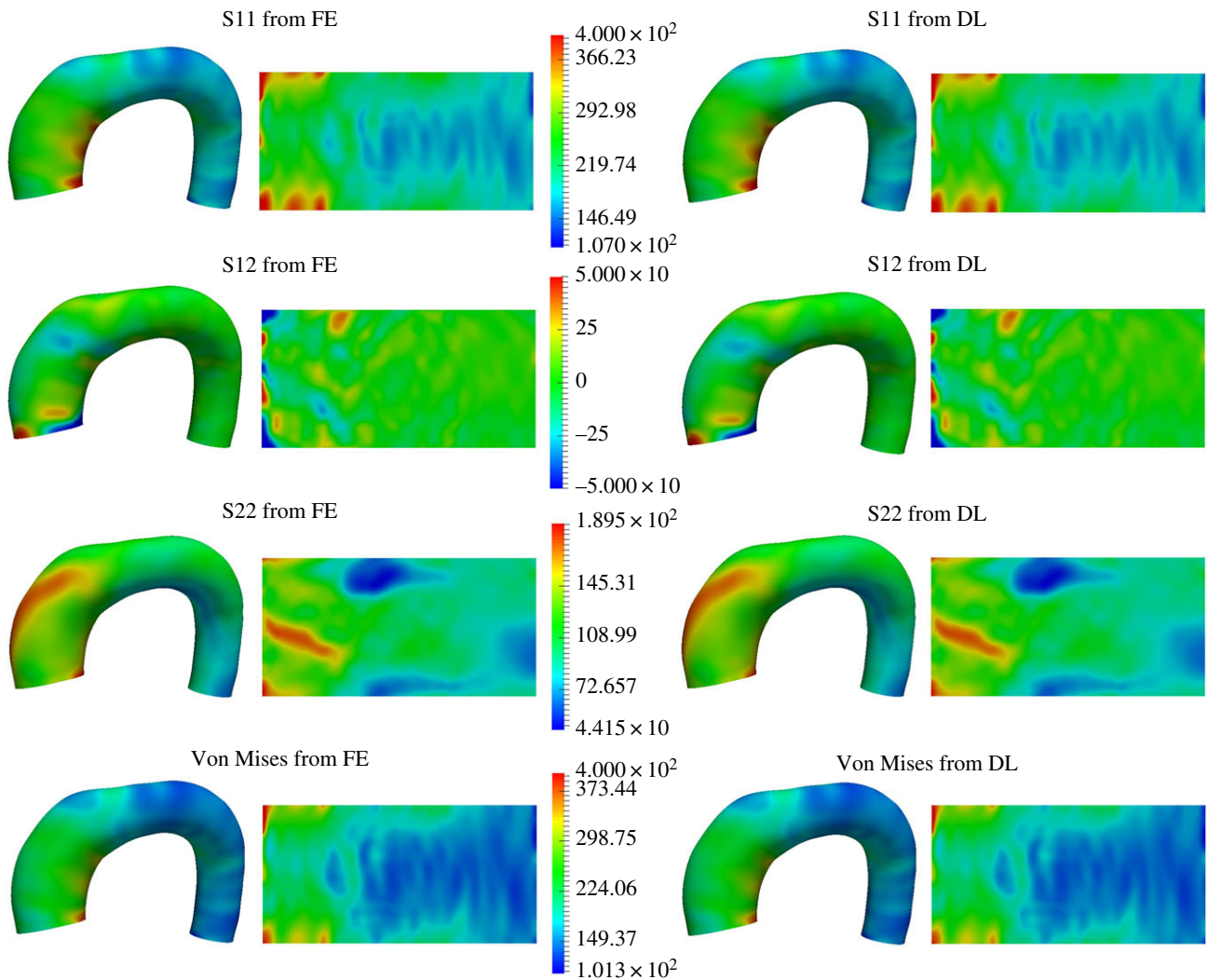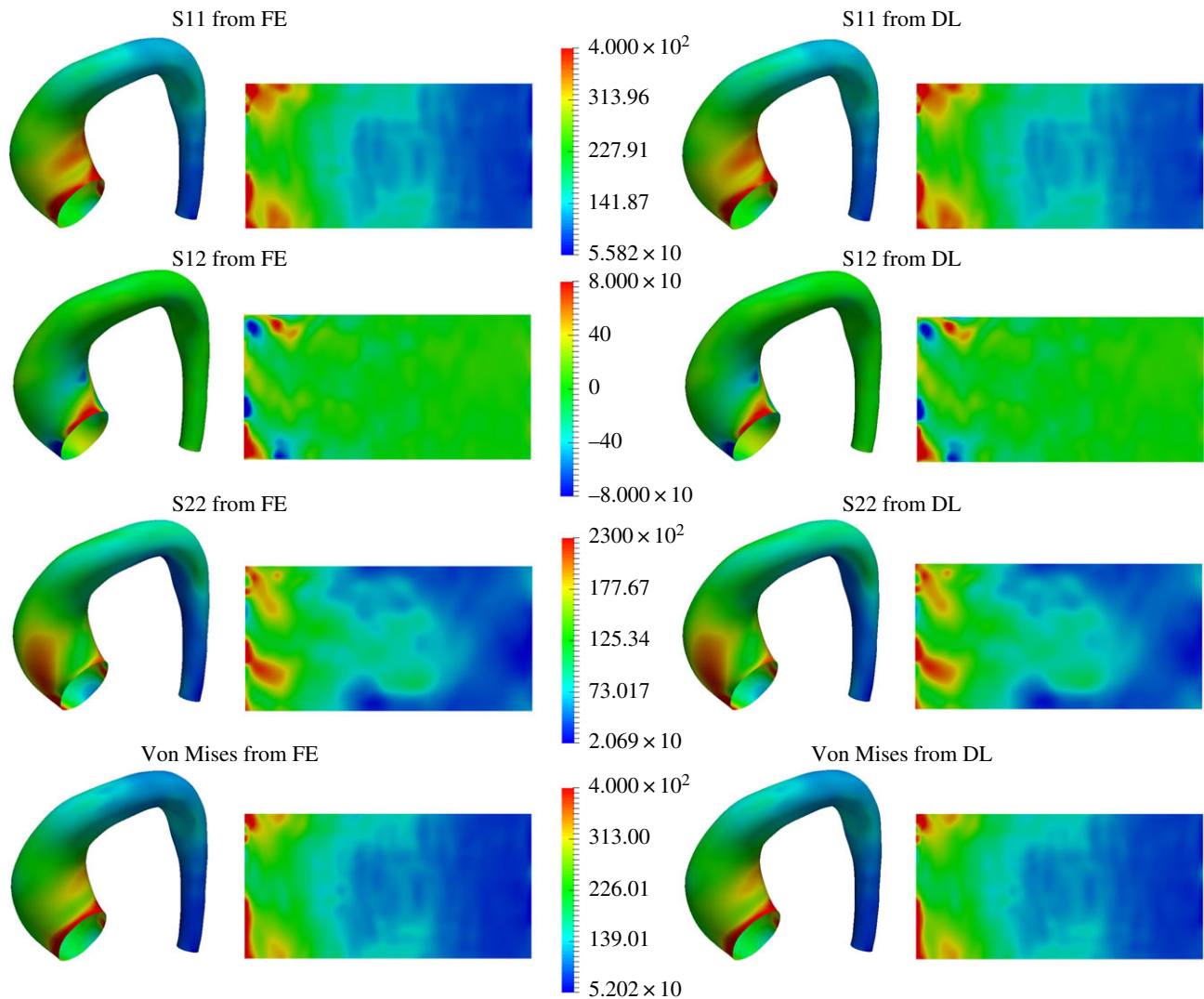
Figure 7. Estimated stress distributions for Patient 1. Units are in KPa. Each stress distribution is mapped into a two-dimensional region (figure 2). The first and the second columns are the stress distributions from finite-element simulation. The middle column shows the stress ranges. The fourth and fifth columns are the stress distributions estimated by the DL model.

dataset obtained from FEA. In both applications, the input to the ML models is geometry information (some features or the entire shape) and the output is a scalar value (FFR or rupture risk). For a complete FE analysis, the output from the ML models must include the entire stress distributions, which demands more complex ML models to describe the relationship between high-dimensional input (5000 nodes) and high-dimensional output (S_{11}, S_{12} and S_{22} on the 5000 nodes). To resolve this challenge, we developed a DL model with three modules, decomposing the whole task into three, easier to handle, sub-tasks. The shape encoding and stress encoding/decoding modules effectively transform the geometry input and the stress output into two compact sets of scalar values which can be handled by a fully connected neural network for nonlinear mapping. To avoid potential overfitting issues and speed up the training process, we used unsupervised learning methods for training the shape encoding module and the stress decoding module.

As the goal of this study was to evaluate the feasibility of using DL techniques to estimate stress distributions, the following simplifications in the FE models were made to facilitate the study: (i) a mean uniform wall thickness was assigned to each of the models; (ii) the branching vessels at the arch were removed; (iii) only one set of constitutive parameters, representing the mean response, was used; and

(iv) residual stress in the wall was not considered. These limitations can be improved in future work. For example, it is possible to obtain the thickness distribution of the aortic wall *in vivo* using advanced magnetic resonance imaging [36]. It is feasible to include the branching vessels in the mesh model by stitching the meshes of branching vessels and the main aorta body together, which requires a substantial amount of programming work on mesh processing [37]. Once the automatic meshing of the whole aorta is realized, shape encoding can be directly applied owing to the power of PCA for shape analysis [26]. To incorporate material properties in the DL model, there are two options: (i) directly use the constitutive model parameters as input to the DL model; or (ii) use the geometries at two cardiac phases as input to the DL model. Based on the study in [38,39], the parameters of a constitutive model can be identified from the aorta shapes at two cardiac phases at known blood pressure levels, which implies that certain material property information is embedded in the two deformed geometries. It should be noted that, for the aortic wall, the stress distributions are almost independent of material properties due to quasi-static determinacy [40–42]. As the average stress through the wall thickness was used in this study, the residual stress should have a minimal effect on the stress distributions on the aorta wall. To incorporate the residual stress for other

Figure 8. Estimated stress distributions for Patient 2. Units are in KPa. Each stress distribution is mapped into a two-dimensional region (figure 2). The first and the second columns are the stress distributions from finite-element simulation. The middle column shows the stress ranges. The fourth and fifth columns are the stress distributions estimated by the DL model.

Table 3. The accuracy of the estimated stress distributions shown in figure 7.

	S_{11}	S_{22}	S_{12}	Von Mises
MAE (KPa)	0.311	0.238	0.440	0.273
NMAE	0.079%	0.134%	1.180%	0.078%

Table 4. The accuracy of the estimated stress distributions shown in figure 8.

	S_{11}	S_{22}	S_{12}	Von Mises
MAE (KPa)	4.335	2.191	0.557	3.822
NMAE	1.123%	1.006%	0.618%	1.131%

applications, several methods in the literature [43,44] which can model residual stress in human organs could be used to generate training data for the DL model. In this application, only the stress distributions at the systolic phase were considered. By performing FE simulations over the whole blood pressure range (e.g. from 10 KPa at diastole to 16 KPa at systole) to generate training data, the stress distributions over the entire cardiac cycle can be 'computed' by a trained DL model.

As a feasibility study, the training and testing data were generated from an SSM using a limited amount of patient data (see appendix); and, therefore, this approach is not ready for clinical applications yet until a large amount of data is collected for training. We note that the SSM has captured some major variations of the aorta, such as the overall changes in size, the diameter variations along the centre line, and the variations in centre-line curvature and surface curvature, as shown in our previous paper [10], and therefore the data are sufficient for this feasibility study. As more data become available, the SSM, after being updated on new data, can still be used to generate FE model shapes in a large range of variations, and the generated shapes may not even be seen in the dataset for building the SSM, which effectively increases the number of training shapes.

Generally, it is possible that an input aorta geometry may be significantly different from those of the training data, which may cause trouble to the DL model. As suggested by a recent work on the relationship between DL and training data [45], this problem can be solved by using more training data and fine-tuning the DL model in our future work. In the case of having extremely unique shapes, a rejection option

[46,47] can be incorporated into the DL model, and the enhanced model can refuse to make an analysis if an input shape is very different from those of the training data. The implementation of the rejection option will be a part of our future work.

Based on the universal approximation theorem (UAT) and its variants [28,48–51] in ML, DNNs have the capability to model complex relationship between the input and the output to FEA for stress analysis, thus serving as a surrogate of FEA. The DL model in this study can be straightforwardly extended for stress analysis of other organs. PCA is a proven method for shape analysis [26], and has been used for modelling the whole heart [52], and its enhanced version [53] has been used for modelling left ventricle dynamics in the whole cardiac cycle. Thus, the shape encoding module is capable of handling more complex geometries. The number of layers and units in the nonlinear mapping module can be configured to handle different lengths of shape code or stress code. In this study, because the aortic wall is modelled using shell elements, the out-of-plane stress components are zero, and thus ignored. For other applications, if necessary, the full stress tensor can be recovered by including all of the stress components in the vector $S^{(k)}$ in equation (2.4). The stress decoding module is capable of reconstructing complex stress distribution from stress code owing to transposed convolution (also known as deconvolution) that has been successfully used for image recognition applications [28,54,55].

We demonstrated that the DL model can 'compute' stress distributions consistent with FEA. The DL model is magnitudes faster than FEA because it directly models the nonlinear and deterministic relationship between the input and the output, avoiding the extensive computations (e.g. numerous Newton–Raphson iterations and time increments) in FEA. The DL model can also be trained for strain estimation given appropriate training data by replacing the output stress with strain. By using GPU computing [31], the DL model can be straightforwardly generalized for other large and complex geometries, while maintaining a similar speed. The fast computational speed of the DL model will enable real-time mechanical analysis, making the potential applications limitless.

This approach will have a substantial impact on medical applications. As the organ geometries (such as the aorta) are similar and the range of material properties (i.e. constitutive parameters) is confined among the patients, statistical modelling and coding of patient characteristics can be performed to build DL models. If enough FEA simulation results are obtained, DL models can be trained and used to predict certain clinical events, such as aortic aneurysm rupture [10] and transcatheter aortic valve replacement (TAVR). Although it seems costly to generate training data from a large number of FE simulations, this approach will enable real-time stress analysis for many clinical applications that are time-sensitive, and thus the benefit is worth the initial investment on FE simulations. For example, our group has used patient-specific structural FEA to study tissue–stent interaction in TAVR [11]. TAVR FEA can predict adverse clinical events such as aortic root rupture due to excessive expansion forces of the stent, but may require days to a week of computing time to complete the analysis, which makes it impractical to use in clinical applications. The DL model presented in this study can be generalized for the TAVR application; and if trained on sufficient FEA data, it

will output the analysis result for the clinicians within minutes if not seconds.

5. Conclusion

We developed the first DL approach for the estimation of stress distributions as a fast and accurate surrogate of FEA, which was demonstrated for the application of stress analysis of the human thoracic aorta. For an input aorta geometry, the trained DL model outputs aortic wall stress distributions in one second, consistent with and magnitudes faster than FEA. This novel approach will enable real-time stress analysis of human organs for numerous clinical applications.

Appendix A

The patient geometry and FE simulation dataset are described in detail in the subsequent sections.

A.1. Patient image data and geometry reconstruction

Cardiac CT images of 25 thoracic aortic aneurysm patients, who underwent elective repair between the years 2008 and 2010, were obtained from Yale-New Haven Hospital [56]. The images were de-identified, and clinical Institutional Review Board approval to review these de-identified images was obtained for this study. The resolution of the images is $0.7 \times 0.7 \times 2.5$ mm, and the field of view covers the thoracic and abdominal aorta. For each patient, the three-dimensional surface of the aorta was semi-automatically reconstructed from the image data, and then it was trimmed at the ascending aorta just distal to the sinotubular junction on the proximal end and at the descending aorta on the distal end. The branch vessels at the arch were removed. The resulting surface was remeshed [10] with the same number of nodes and elements (i.e. 5000 nodes and 4950 elements), which established mesh correspondence between different patients. As shown in figure 2, each aorta mesh can be cut along the longitudinal direction, and the resulting mesh is topologically equivalent to a flat rectangular mesh.

A.2. Patient geometry data

A SSM [10] was built from the patient data to generate a large number of virtual aorta geometries, which will augment the dataset and facilitate the DL application. Briefly, the patient aorta shapes were aligned to a common coordinate system by Generalized Procrustes Analysis [57]. Then PCA [26,58] was invoked to build the SSM from these aligned shapes, which consists of a mean shape $\bar{X}$, eigenvectors $\{W_m\}$

(i.e. modes of shape variations) and eigenvalues $\{\lambda_m\}$ of the covariance matrix. Using the SSM, a shape X can be represented by using equation (2.1). In this study, the first three modes were selected ($M = 3$), which explains 80.1% of the total variation. A total number of 729 shapes were obtained by uniformly sampling the parameters $\{\alpha_1, \alpha_2, \alpha_3\}$ in the range of -2 to 2, i.e. within 2 standard deviations of the mean shape. Therefore, each of the 729 shapes can be considered to represent a virtual patient.

A.3. Stress data from finite-element simulation

FEA was performed on each of the 729 shapes to obtain the stress distributions on the aortic wall, using Abaqus/Standard 6.14 (Simulia, RI). The backward displacement method [10] was used to estimate the unpressurized geometry, and then each unpressurized geometry was inflated under the systolic pressure of 16 kPa. In the simulations, S4R shell elements were used, and the aortic wall was prescribed a uniform thickness of 2 mm [56] at the unpressurized state, which is the mean thickness based on our experimental data [59]. While assumed thickness is a limitation, it is currently not possible to measure wall thickness from CT images due to the partial volume effect [60] and poor image contrast on vessel tissue. A fibre-reinforced hyperelastic material model based on the work of Gasser *et al.* [24] was used to characterize the aortic wall mechanical

response. The strain energy function can be expressed as

$$
\Psi = C_{10}(\bar{I}_1 - 3) \\
+ \frac{k_1}{2k_2} \sum_{i=1}^{2} [\exp\{k_2[\kappa \bar{I}_1 + (1 - 3\kappa)\bar{I}_{4i} - 1]^2\} - 1], \quad \text{(A 1)}
$$

where C_{10} is material parameter to describe the matrix material and k_1 is a positive material parameter that has the same unit of stress, while k_2 is a unitless parameter. The strain invariant $\bar{I}_1$ characterizes the matrix material; and the strain invariant $\bar{I}_{4i}$ characterizes the fibre families. $\bar{I}_{4i}$ is equal to squares of the stretches in the fibre directions and κ is a dispersion parameter describing the distribution of fibre orientation. A parameter θ defines the angle between the mean local fibre direction and the circumferential axis of the local coordinate system. The constitutive parameters in this model were prescribed based on our previous experiment [25]: $C_{10} = 27.91, k_1 = 512.56, k_2 = 2.561 \times 10^{-8}, \kappa = 0.3190, \theta = 90$.

In all simulations, pressures were applied uniformly to the inner surface of the aorta models, and the boundary nodes of the aorta models, i.e. the proximal and distal ends of the model, were only allowed to move in the radial direction based on the local coordinate system. Once the simulation for a shape was completed, the stress values at each node were output from Abaqus and the average stress components across the thickness were calculated.

References

1. Auricchio F, Conti M, Morganti S, Reali A. 2014 Simulation of transcatheter aortic valve implantation: a patient-specific finite element approach. *Comput. Methods Biomech. Biomed. Engin.* **17**, 1347–1357. (doi:10.1080/10255842.2012.746676)

2. Capelli C, Bosi GM, Cerri E, Nordmeyer J, Odenwald T, Bonhoeffer P, Migliavacca F, Taylor AM, Schievano S. 2012 Patient-specific simulations of transcatheter aortic valve stent implantation. *Med. Biol. Eng. Comput.* **50**, 183–192. (doi:10.1007/s11517-012-0864-1)

3. Dwyer HA, Matthews PB, Azadani A, Ge L, Guy TS, Tseng EE. 2009 Migration forces of transcatheter aortic valves in patients with noncalcific aortic insufficiency. *J. Thorac. Cardiovasc. Surg.* **138**, 1227–1233. (doi:10.1016/j.jtcvs.2009.02.057)

4. Morganti S, Conti M, Aiello M, Valentini A, Mazzola A, Reali A, Auricchio F. 2014 Simulation of transcatheter aortic valve implantation through patient-specific finite element analysis: two clinical cases. *J. Biomech.* **47**, 2547–2555. (doi:10.1016/j.jbiomech.2014.06.007)

5. Wang Q, Kodali S, Primiano C, Sun W. 2015 Simulations of transcatheter aortic valve implantation: implications for aortic root rupture. *Biomech. Model. Mechanobiol.* **14**, 29–38. (doi:10.1007/s10237-014-0583-7)

6. Wang Q, Sirois E, Sun W. 2012 Patient-specific modeling of biomechanical interaction in transcatheter aortic valve deployment. *J. Biomech.*

45, 1965–1971. (doi:10.1016/j.jbiomech.2012.05.008)

7. Morganti S, Brambilla N, Petronio AS, Reali A, Bedogni F, Auricchio F. 2015 Prediction of patient-specific post-operative outcomes of TAVI procedure: the impact of the positioning strategy on valve performance. *J. Biomech.* **49**, 2513–2519. (doi:10.1016/j.jbiomech.2015.10.048)

8. Jaegere PD, *et al.* 2016 Patient-specific computer modeling to predict aortic regurgitation after transcatheter aortic valve replacement. *JACC Cardiovasc. Interv.* **9**, 508–512. (doi:10.1016/j.jcin.2016.01.003)

9. Sun W, Martin C, Pham T. 2014 Computational modeling of cardiac valve function and intervention. *Annu. Rev. Biomed. Eng.* **16**, 53–76. (doi:10.1146/annurev-bioeng-071813-104517)

10. Liang L, Liu M, Martin C, Elefteriades JA, Sun W. 2017 A machine learning approach to investigate the relationship between shape features and numerically predicted risk of ascending aortic aneurysm. *Biomech. model. mechanobiol.* **16**, 1519–1533. (doi:10.1007/s10237-017-0903-9)

11. Wang Q, Primiano C, McKay R, Kodali S, Sun W. 2014 CT image-based engineering analysis of transcatheter aortic valve replacement. *JACC Cardiovasc. Imaging* **7**, 526–528. (doi:10.1016/j.jcmg.2014.03.006)

12. Liang L, Kong F, Martin C, Pham T, Wang Q, Duncan J, Sun W. 2017 Machine learning–based 3-D geometry reconstruction and modeling of aortic

valve deformation using 3-D computed tomography images. *Int. J. Numer. Methods Biomed. Eng.* **33**, e2827. (doi:10.1002/cnm.2827)

13. Zhang S, Zhan Y, Metaxas DN. 2012 Deformable segmentation via sparse representation and dictionary learning. *Med. Image Anal.* **16**, 1385–1396. (doi:10.1016/j.media.2012.07.007)

14. Staib LH, Duncan JS. 1996 Model-based deformable surface finding for medical images. *IEEE Trans. Med. Imaging* **15**, 720–731. (doi:10.1109/42.538949)

15. Yang J, Duncan JS. 2004 3D image segmentation of deformable objects with joint shape-intensity prior models using level sets. *Med. Image Anal.* **8**, 285–294. (doi:10.1016/j.media.2004.06.008)

16. Pouch AM, Wang H, Takabe M, Jackson BM, Gorman III JH, Gorman RC, Yushkevich PA, Sehgal CM. 2014 Fully automatic segmentation of the mitral leaflets in 3D transesophageal echocardiographic images using multi-atlas joint label fusion and deformable medial modeling. *Med. Image Anal.* **18**, 118–129. (doi:10.1016/j.media.2013.10.001)

17. Yu Y, Zhang S, Huang J, Metaxas D, Axel L. 2013 Sparse deformable models with application to cardiac motion analysis. In *Information processing in medical imaging* (eds J Gee, S Joshi, K Pohl, W Wells, L Zöllei), pp. 208–219. Berlin, Germany: Springer Berlin Heidelberg.

18. Litjens G, Kooi T, Bejnordi BE, Setio AAA, Ciompi F, Ghafoorian M, van der Laak JAWM, van Ginneken B, Sánchez CI. 2017 A survey on deep learning in

medical image analysis. *Med. Image Anal.* **42**, 60–88. (doi:10.1016/j.media.2017.07.005)

19. Ronneberger O, Fischer P, Brox T. 2015 U-Net: convolutional networks for biomedical image segmentation. In *Medical Image Computing and Computer-assisted Intervention – MICCAI 2015: 18th Int. Conf., Munich, Germany, October 5–9, 2015, Proceedings, Part III* (eds N Navab, J Hornegger, WM Wells, AF Frangi), pp. 234–241. Cham, Switzerland: Springer International Publishing.

20. Milletari F, Navab N, Ahmadi SA. 2016 V-Net: fully convolutional neural networks for volumetric medical image segmentation, 2016. In *Fourth Int. Conf. on 3D vision* (3DV), *Stanford, CA, 25–28 October*, pp. 565–571. Piscataway, NJ: IEEE.

21. Zheng Y, John M, Liao R, Nöttling A, Boese J, Kempfert J, Walther T, Brockmann G, Comaniciu D. 2012 Automatic aorta segmentation and valve landmark detection in C-arm CT for transcatheter aortic valve implantation. *IEEE Trans. Med. Imaging* **31**, 2307–2321. (doi:10.1109/TMI.2012.2216541)

22. LeCun Y, Bengio Y, Hinton GE. 2015 Deep learning. *Nature* **521**, 436–444. (doi:10.1038/nature14539)

23. Schmidhuber J. 2015 Deep learning in neural networks: an overview. *Neural Netw.* **61**, 85–117. (doi:10.1016/j.neunet.2014.09.003)

24. Gasser TC, Ogden RW, Holzapfel GA. 2006 Hyperelastic modelling of arterial layers with distributed collagen fibre orientations. *J. R. Soc. Interface* **3**, 15–35. (doi:10.1098/rsif.2005.0073)

25. Martin C, Sun W, Pham T, Elefteriades J. 2013 Predictive biomechanical analysis of ascending aortic aneurysm rupture potential. *Acta Biomater.* **9**, 9392–9400. (doi:10.1016/j.actbio.2013.07.044)

26. Heimann T, Meinzer H-P. 2009 Statistical shape models for 3D medical image segmentation: a review. *Med. Image Anal.* **13**, 543–563. (doi:10.1016/j.media.2009.05.004)

27. Dugas C, Bengio Y, Bélisle F, Nadeau C, Garcia R. 2000 Incorporating second-order functional knowledge for better option pricing. In *Proc. of the 13th Int. Conf. on Neural Information Processing Systems, Denver, CO*, pp. 451–457. Cambridge, MA: MIT Press.

28. Goodfellow I, Bengio Y, Courville A. 2016 *Deep learning*. Cambridge, MA: The MIT Press.

29. Markovsky I. 2008 Structured low-rank approximation and its applications. *Automatica* **44**, 891–909. (doi:10.1016/j.automatica.2007.09.011)

30. Kingma DP, Ba J. 2015 *Adam: a method for stochastic optimization*. The 3rd international conference for learning representations, San Diego, CA, 7–9 May. ICLR.

31. Abadi M *et al.* 2015 TensorFlow: large-scale machine learning on heterogeneous distributed systems. (http://tensorflow.org/)

32. Tompson J, Schlachter K, Sprechmann P, Perlin K. 2017 Accelerating eulerian fluid simulation with convolutional networks. In *Proc. of the 34th int. conf. on Machine Learning, PMLR* (eds P Doina, T Yee Whye), *Sydney, Australia, 6–11 August*, pp. 3424–3433. PMLR

33. Hennigh O. 2017 Lat-Net: Compressing lattice Boltzmann flow simulations using deep neural networks. (https://arxiv.org/abs/1705.09036)

34. Guo X, Li W, Iorio F. 2016 Convolutional neural networks for steady flow approximation. In *Proc. of the 22nd ACM SIGKDD Int. Conf. on Knowledge Discovery and Data Mining, San Francisco, CA, 13–17 August*, pp. 481–490. New York, NY: ACM.

35. Itu L, Rapaka S, Passerini T, Georgescu B, Schwemmer C, Schoebinger M, Flohr T, Sharma P, Comaniciu D. 2016 A machine-learning approach for computation of fractional flow reserve from coronary computed tomography. *J. Appl. Physiol.* **121**, 42–52. (doi:10.1152/japplphysiol.00752.2015)

36. Dieleman N, van der Kolk AG, Zwanenburg JJM, Harteveld AA, Biessels GJ, Luijten PR, Hendrikse J. 2014 Imaging intracranial vessel wall pathology with magnetic resonance imaging. *Circulation* **130**, 192. (doi:10.1161/CIRCULATIONAHA.113.006919)

37. Botsch M, Kobbelt L, Pauly M, Alliez P, Levy B. 2010 Polygon Mesh Processing, A K Peters/CRC Press.

38. Wittek A, Karatolios K, Bihari P, Schmitz-Rixen T, Moosdorf R, Vogt S, Blase C. 2013 In vivo determination of elastic properties of the human aorta based on 4D ultrasound data. *J. Mech. Behav. Biomed. Mater.* **27**, 167–183. (doi:10.1016/j.jmbbm.2013.03.014)

39. Wittek A, Derwich W, Karatolios K, Fritzen CP, Vogt S, Schmitz-Rixen T, Blase C. 2016 A finite element updating approach for identification of the anisotropic hyperelastic properties of normal and diseased aortic walls from 4D ultrasound strain imaging. *J. Mech. Behav. Biomed. Mater.* **58**, 122–138. (doi:10.1016/j.jmbbm.2015.09.022)

40. Liu M, Liang L, Sun W. 2017 A new inverse method for estimation of in vivo mechanical properties of the aortic wall. *J. Mech. Behav. Biomed. Mater.* **72**, 148–158. (doi:10.1016/j.jmbbm.2017.05.001)

41. Joldes GR, Miller K, Wittek A, Doyle B. 2016 A simple, effective and clinically applicable method to compute abdominal aortic aneurysm wall stress. *J. Mech. Behav. Biomed. Mater.* **58**, 139–148. (doi:10.1016/j.jmbbm.2015.07.029)

42. Miller K, Lu J. 2013 On the prospect of patient-specific biomechanics without patient-specific properties of tissues. *J. Mech. Behav. Biomed. Mater.* **27**, 154–166. (doi:10.1016/j.jmbbm.2013.01.013)

43. Pierce DM, Fastl TE, Rodriguez-Vila B, Verbrugghe P, Fourneau I, Maleux G, Herijgers P, Gomez EJ, Holzapfel GA. 2015 A method for incorporating three-dimensional residual stretches/stresses into patient-specific finite element simulations of arteries. *J. Mech. Behav. Biomed. Mater.* **47**, 147–164. (doi:10.1016/j.jmbbm.2015.03.024)

44. Genet M, Rausch MK, Lee LC, Choy S, Zhao X, Kassab GS, Kozerke S, Guccione JM, Kuhl E. 2015 Heterogeneous growth-induced prestrain in the heart. *J. Biomech.* **48**, 2080–2089. (doi:10.1016/j.jbiomech.2015.03.012)

45. Sun C, Shrivastava A, Singh S, Gupta A. 2017 Revisiting unreasonable effectiveness of data in deep learning era. (https://arxiv.org/abs/1707.02968)

46. Bartlett PL, Wegkamp MH. 2008 Classification with a reject option using a hinge loss. *J. Mach. Learn. Res.* **9**, 1823–1840.

47. Geifman Y, El-Yaniv R. 2017 Selective classification for deep neural networks. (https://arxiv.org/abs/1705.08500)

48. Cybenko G. 1989 Approximation by superpositions of a sigmoidal function, mathematics of control. *Signals Syst.* **2**, 303–314. (doi:10.1007/BF02551274)

49. Sonoda S, Murata N. 2017 Neural network with unbounded activation functions is universal approximator. *Appl. Comput. Harmon. Anal.* **43**, 233–268. (doi:10.1016/j.acha.2015.12.005)

50. Shaham U, Cloninger A, Coifman RR. In press. Provable approximation properties for deep neural networks. *Appl. Comput. Harmon. Anal.* (https://arxiv.org/abs/1509.07385)

51. Hornik K. 1991 Approximation capabilities of multilayer feedforward networks. *Neural Netw.* **4**, 251–257. (doi:10.1016/0893-6080(91)90009-T)

52. Zheng Y, Barbu A, Georgescu B, Scheuering M, Comaniciu D. 2008 Four-chamber heart modeling and automatic segmentation for 3-D cardiac CT volumes using marginal space learning and steerable features. *IEEE Trans. Med. Imaging* **27**, 1668–1681. (doi:10.1109/TMI.2008.2004421)

53. Zhu Y, Papademetris X, Sinusas AJ, Duncan JS. 2010 Segmentation of the left ventricle from cardiac MR images using a subject-specific dynamical model. *IEEE Trans. Med. Imaging* **29**, 669–687. (doi:10.1109/TMI.2009.2031063)

54. Dumoulin V, Belghazi I, Poole B, Mastropietro O, Lamb A, Arjovsky M, Courville A. 2017 Adversarially learned inference. In *Int. Conf. on Learning Representations Toulon, France, 24–26 April*. ICLR.

55. Zeiler MD, Taylor GW, Fergus R. 2011 Adaptive deconvolutional networks for mid and high level feature learning. *2011 Int. Conf. on computer vision, Barcelona, Spain, 6–13 November*, pp. 2018–2025. Piscataway, NJ: IEEE.

56. Martin C, Sun W, Elefteriades J. 2015 Patient-specific finite element analysis of ascending aorta aneurysms. *Am. J. Physiol. Heart Circ. Physiol.* **308**, 1306–1316. (doi:10.1152/ajpheart.00908.2014)

57. Goodall C. 1991 Procrustes methods in the statistical analysis of shape. *J. R. Stat. Soc. B* **53**, 285–339.

58. Cootes TF, Taylor CJ, Cooper DH, Graham J. 1995 Active shape models - their training and application. *Comput. Vis. Image Underst.* **61**, 38–59. (doi:10.1006/cviu.1995.1004)

59. Pham T, Martin C, Elefteriades J, Sun W. 2013 Biomechanical characterization of ascending aortic aneurysm with concomitant bicuspid aortic valve and bovine aortic arch. *Acta Biomater.* **9**, 7927–7936. (doi:10.1016/j.actbio.2013.04.021)

60. Barrett JF, Keat N. 2004 Artifacts in CT: recognition and avoidance. *Radiographics* **24**, 1679–1691. (doi:10.1148/rg.246045065)